



ARTICLE

Directional Explosion of Finite Volume Water Confined in a Single-End-Opened CNT

Jiahao Liu^{1,#}, Yuanyuan Kang^{2,#}, Kun Cai^{2,*}, Haiyan Duan¹ and Jiao Shi^{3,*}

¹School of Forestry, Northwest A&F University, Yangling, 712100, China

²School of Science, Harbin Institute of Technology, Shenzhen, 518055, China

³College of Water Resources and Architectural Engineering, Northwest A&F University, Yangling, 712100, China

*Corresponding Authors: Kun Cai. Email: kun.cai@hit.edu.cn; Jiao Shi. Email: shijiaoau@163.com

#These authors contributed equally to this work

Received: 02 April 2025; Accepted: 15 May 2025; Published: 03 July 2025

ABSTRACT: The directional explosion behavior of finite volume water confined within nanochannels holds considerable potential for applications in precision nanofabrication and bioengineering. However, precise control of nanoscale mass transfer remains challenging in nanofluidics. This study examined the dynamic evolution of water clusters confined within a single-end-opened carbon nanotube (CNT) under pulsed electric field (EF) excitation, with a particular focus on the structural reorganization of hydrogen bond (H-bond) networks and dipole orientation realignment. Molecular dynamics simulations reveal that under the influence of pulsed EF, the confined water molecules undergo cooperative restructuring to maximize hydrogen bond formation through four independent motions during deformation, such as waving, spinning, axial slipping, and radial migration. In this process, the dynamic fracture and recombination of the hydrogen bond network generate an instantaneous high pressure, and drive a unidirectional explosion along the CNT axis. A smaller CNT diameter or a reduced water volume under the same EF conditions leads to a stronger explosion. In contrast, in a wider CNT, the water cluster expands axially and forms a cylindrical shell whose thickness gradually decreases as the axial expansion slows. These insights offer precise control strategies for nanofluidic systems in nanofabrication or bioengineering applications, where finite volume water serves as a programmable nanoscale energy transfer medium.

KEYWORDS: Finite volume water; mass transfer; directional explosion; electric field; molecular dynamics

1 Introduction

Nanoscale mass transfer has been widely observed in fields such as biomedicine [1–3], energy conversion [4,5], and environmental governance [6,7]. For example, Khatibi et al. [8] were inspired by various nanostructures and designed pH-regulated nanochannels that could be employed for seawater desalination. It has garnered significant attention in both experimental and theoretical research, though many challenges remain. A key issue is the precise control of the movement path and speed of the carrier, which is particularly important for drug delivery processes [9–11]. Typically, a carrier is placed in a liquid-filled nanochannel to provide propulsion [5,12,13]. At present, a considerable number of studies have disclosed the transport behavior of water or ions in nanochannels. Heydari et al. [14] investigated the ion transport behavior in a mixed nanochannel composed of two cones and one cylinder and explored the influence of the length of each part on the ion transport behavior of the nanochannel via numerical simulation methods. However, carbon nanotubes (CNTs) [15,16], a prominent type of nanochannel, show great potential for applications in drug



delivery, seawater desalination, biosensing, and other areas [17–19]. The nanoflow of water confined within CNTs was first studied by Hummer et al. [20], who demonstrated the formation of one-dimensional ordered water chains, laying the groundwork for understanding water transport in nanochannels and enabling pulsed high-speed water transfer. Due to the nanoscale geometric constraints and ultra-low friction properties of CNTs, water flows through these tubes at rates four to five orders of magnitude faster than predicted by conventional fluid dynamics theory [21,22].

The dynamic behavior of water molecules in CNTs has been studied through various approaches, including the manipulation of CNT size and the application of external electric fields (EFs). At the nanoscale, the structure and dynamics of water molecules differ significantly from those in macroscopic systems [23]. For instance, the continuum hypothesis for water flow was proposed when CNT diameters exceed 1.39 nm [24]. However, in CNTs with diameters under 2 nm, water flow velocities have been shown to exceed predictions from fluid dynamics models by more than three orders of magnitude, aligning instead with molecular dynamics simulation results [25,26]. Thomas et al. [27] further employed molecular dynamics simulations to reevaluate pressure-driven flows in CNTs with diameters from 1.66 to 4.99 nm, finding substantial deviations from experimental data [21]. This discrepancy may stem from uncontrolled external forces, such as electric fields, or inaccuracies in calculating flow areas. Recent studies [28] suggest that the anomalous water transport in narrow CNTs (0.83 nm diameter) is closely linked to a dynamic hydrogen bond chain connecting water molecules within and outside the CNT. Notably, as CNT length increases, water flow rates initially rise before either stabilizing or decreasing.

The structural evolution of confined water has been extensively studied. Srivastava et al. [29] observed that at a low temperature of 271 K, the diffusion behavior of water molecules deviates from the Arrhenius law [30], indicating that the diffusion coefficient does not follow an exponential temperature relationship. Song et al. [31] explored the spontaneous water filling of CNTs with diameters ranging from 8.14 to 20.35 Å and found that water molecules in the bulk phase must disrupt their hydrogen bond network and overcome an energy barrier to enter the CNTs. These factors contribute to an entrance resistance, resulting in a threefold increase in water flux.

Due to their polarity, water molecules can be directionally regulated by an electric field (EF) through induced dipole orientation [32]. Numerous studies have shown that an axial EF effectively enhances water flux in CNTs [33,34], including those with hourglass-shaped structures [35]. For example, a transverse EF causes a linear decrease in water molecule flux, approaching zero at a certain field intensity [36]. Ostler et al. [37] leveraged the interaction between water molecules' dipole moments and a rotating electric field (REF) to induce forward water flow within CNTs. Additionally, Cai et al. [38] developed a rotary nanomotor submerged in water and exposed to an REF, while Kang et al. [39] created a water-filled CNT motor driven by an REF. Salman et al. [40] demonstrated the effect of temperature on the coupled transport of hydrated ions in CNTs under an EF.

However, the aforementioned studies have predominantly focused on the transport mechanisms of continuous water flow in open-ended CNTs, while the directional explosion of finite volume water confined within single-end-opened CNTs and its geometric modulation mechanisms remain unrevealed. To address this, Kang et al. [41] developed a nano-ejector model, and introduced an external rotating electric field (REF) to trigger the water cluster's deformation to push a graphene flake out of the CNT. However, the graphene flake showed noticeable deformation and lateral rotation during ejection and lacked the capacity to encapsulate materials such as drug particles. Therefore, Duan et al. [42] opted to use a nanocapsule instead of graphene flake to cover the water cluster and evaluate the effect of EF on the nanocapsule's exit velocity. However, two questions remain unanswered: How does the water structure evolve during an explosion? And

how to control the unidirectional explosion? This study will address these two questions for the potential application of directional explosion in mass transfer at the nanoscale.

2 Model and Methodology

2.1 A Model for Testing Nano-Explosion

Fig. 1 shows a model for testing the explosion of finite volume water within a single-end-opened single-walled carbon nanotube (SWCNT). The SWCNT has four options: SWCNT (50, 50), (40, 40), (30, 30), or (20, 20), corresponding to diameters of $1.0d = 67.8 \text{ \AA}$, $0.8d = 54.2 \text{ \AA}$, $0.6d = 40.7 \text{ \AA}$, and $0.4d = 27.1 \text{ \AA}$, respectively (Table S1). For simplicity, these models are named 1.0d-CNT, 0.8d-CNT, 0.6d-CNT, and 0.4d-CNT. When the water depth (H) is 70 \AA , the four models contain 5716, 3252, 1459, and 824 water molecules, respectively. In this study, the nanocapsule has a thickness of 17 \AA . The axial direction of the SWCNT outlet is designated as the z -axis (forward direction).

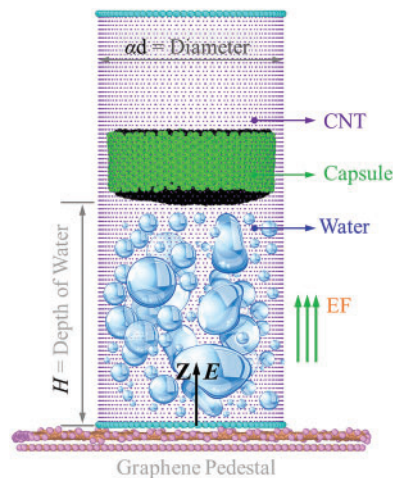


Figure 1: Schematic diagram of the model for measuring the unidirectional explosion. The external pulsed electric field (EF) has an intensity of E . In this model, a water cluster with depth of H is confined in a 120 \AA -long single-end-opened single-walled carbon nanotube (SWCNT) with diameter αd , a two-layered graphene pedestal covering the SWCNT bottom, and a nanocapsule made of a short SWCNT with both ends sealed covers the water cluster

2.2 Methodology

The dynamic response of the current nanosystem is investigated using molecular dynamics (MD) simulations, conducted with the open-source software LAMMPS (Large-scale Atomic/Molecular Massively Parallel Simulator) [43]. This study employs the SPC/E water model [44], with the SHAKE algorithm [45] used to constrain the O-H bond length (1.0 \AA) and H-O-H bond angle (109.47°) of water molecules. Each oxygen and hydrogen atom in a water molecule carries charges of $-0.8476 e$ and $0.4238 e$, respectively. The AIREBO potential function [46] is utilized to describe carbon-carbon (C-C) and carbon-hydrogen (C-H) interactions in various carbon components, including graphene substrates, nanocapsules, and CNT. For non-bonded interactions, the Lennard-Jones potential, based on the Lorentz-Berthelot mixing rules [47], is applied with $\epsilon_{C-O} = 5.0113 \text{ meV}$, $\sigma_{C-O} = 3.2830 \text{ \AA}$, $\epsilon_{O-O} = 6.7343 \text{ meV}$, and $\sigma_{O-O} = 3.1660 \text{ \AA}$ [48], with a cutoff of 12 \AA . The particle-particle-particle mesh (PPPM) method is used to compute long-range electrostatic interactions.

The total potential energy (U_{Total}) of the system is described using a multi-scale potential energy framework. Specifically, the AIREBO potential energy (U_{AIREBO}) that describes short-range chemical interactions between atoms is coupled with the Coulomb potential energy (U_{Coulomb}) that characterizes the electrostatic interactions of charged particles to construct a composite potential energy function, whose mathematical expression is:

$$U_{\text{Total}} = U_{\text{AIREBO}} + U_{\text{Coulomb}}. \quad (1)$$

The U_{AIREBO} combines short-range bond potential, long-range Lennard Jones (LJ) interaction, and dihedral twist potential, as expressed in equation:

$$U_{\text{AIREBO}} = \frac{1}{2} \sum_i \sum_{j \neq i} \left[U_{ij}^{\text{REBO}} + U_{ij}^{\text{LJ}} + \sum_{k \neq i, j} \sum_{l \neq i, j, k} U_{ijkl}^{\text{tors}} \right], \quad (2)$$

where U_{ij}^{REBO} represents the formation and breaking of covalent bonds between atoms; U_{ij}^{LJ} and U_{ijkl}^{tors} adds switch functions $S'(t)$ and weight coefficient judgments w on the basis of its original function, as follows:

$$\begin{cases} U_{ij}^{\text{LJ}} = S'(t_r(r_{ij})) S'(t_b(b_{ij}^*)) C_{ij} V_{ij}^{\text{LJ}}(r_{ij}) + [1 - S'(t_r(r_{ij}))] C_{ij} V_{ij}^{\text{LJ}}(r_{ij}), \\ S'(t) = \Theta(-t) + \Theta(t) \Theta(1-t) [1 - t^2 (3 - 2t)], \\ C_{ij} = 1 - \max \{ w_{ij}(r_{ij}), w_{ik}(r_{ik}) w_{kj}(r_{kj}), \forall k, w_{ik}(r_{ik}) w_{kl}(r_{kl}) w_{lj}(r_{lj}), \forall k, l \}, \\ U_{ijkl}^{\text{tors}} = w_{ki}(r_{ki}) w_{ij}(r_{ij}) w_{jl}(r_{jl}) V^{\text{tors}}(\omega_{ijkl}). \end{cases} \quad (3)$$

The calculation formula for U_{Coulomb} is as follows:

$$U_{\text{Coulomb}} = \frac{1}{4\pi\epsilon_0} \sum_{i < j} \frac{q_i q_j}{r_{ij}}, \quad (4)$$

where $\frac{1}{4\pi\epsilon_0}$ represents the electrostatic constant, q_i and q_j are the charges carried by particles i and j , respectively.

The initial position information r , initial velocity information v and atomic mass m of the structure are known. Then, for the specific dynamic processes of molecules, classical Newtonian mechanics needs to be used for expression:

$$\mathbf{F}_i = m_i \mathbf{a}_i. \quad (5)$$

According to the principles of classical mechanics, the force acting on a single particle in a system can be described by the negative gradient of the potential energy function, i.e.,

$$\mathbf{F}_i = -\nabla U_i. \quad (6)$$

In addition, the updated expressions for the position and velocity of particles are as follows:

$$\begin{cases} \mathbf{v}_i = \int^t \mathbf{a}_i dt = \mathbf{v}'_i + \mathbf{a}_i t, \\ \mathbf{r}_i = \int^t \mathbf{v}_i dt = \mathbf{r}'_i + \mathbf{v}'_i t + \frac{1}{2} \mathbf{a}_i t^2. \end{cases} \quad (7)$$

The acceleration of atomic motion is represented by \mathbf{a} . The position and velocity of atom i at the next moment can be obtained by integrating the acceleration \mathbf{a}_i with time step t . \mathbf{v}'_i and \mathbf{r}'_i represent the initial velocity and initial position of atom i , respectively. Molecular dynamics is a computational methodology

that relies on iterative algorithms to precisely determine the instantaneous positions and velocities of atoms within a system at any specified time point.

Each simulation includes the following essential steps:

Step 1. Construct the system model and set initial parameters for calculation.

Step 2. Reshape the system boundaries by minimizing potential energy.

Step 3. Fix the graphene pedestal, the shell of the nanocapsule, and both ends of the channel, then relax the system under an NVT ensemble (constant atom number N ; constant volume $V = 500 \times 500 \times 1250 \text{ \AA}^3$; and constant temperature $T = 300 \text{ K}$) for 100 ps.

Step 4. After relaxation, release the nanocapsule and activate the pulsed electric field (EF) for a specified period, then deactivate.

Step 5. Collect essential data for post-processing.

In the simulation, the integration time step is set to 0.001 ps, and periodic boundary conditions are applied in all three dimensions of the simulation box. The system temperature is maintained at 300 K using a Nose-Hoover thermostat [49]. A transient electric field (EF) with rectangular pulse intensity is introduced into the nanosystem, where the constant EF intensity, denoted as E , is applied between $[0, s]$ ps, and is directed along the axial direction of the CNT barrel. The exit velocity of the bullet, v_{out} , is recorded for analysis.

The water cluster contains a large number of hydrogen bonds (H-bonds). A hydrogen bond (H-bond) forms between the i th and j th water molecules, denoted as $(\text{O-H})_i \rightarrow \text{O}_j$. The spatial distribution of these bonds must meet two criteria: the distance between O_i and O_j should be less than 3.5 \AA , and the angle of $(\text{O-H})_i \cdots \text{O}_j$ must be $\leq 30^\circ$ [50]. The number of H-bonds per water molecule, denoted as N_{HB} , will be calculated in the simulation to illustrate the structural evolution of the water cluster.

3 Results and Discussion

3.1 Water Explosion in Different-Sized CNTs

We calculate the number of hydrogen bonds (H-bonds) per water molecular (N_{HB}) in each of the four models (see Table S1) over the first 20 ps ($s = 20$ ps). As shown in Fig. 2, the N_{HB} in the 0.4d-CNT model decreases gradually. This trend implies that the motion of the water molecules becomes more random, while simultaneously, the water cluster elongates when the electric field (EF) is activated at $E = 5 \text{ V/\AA}$ for 20 ps.

In the remaining three cases, the value of N_{HB} initially decreases, then increases from a minimum point, eventually tending toward convergence. For instance, in the 0.6d-CNT model, the value of N_{HB} reaches its minimum at 6.7 ps, indicating an increase in broken H-bonds as the EF begins to reorient the water molecules. During this time, the water cluster elongates by about 20 \AA (see Fig. S1b). After approximately 6.7 ps but before 10 ps, the value of N_{HB} increases, demonstrating a reassembly of H-bonds within the deforming water structure. In this period, water molecules with dipole moments aligned along the z -direction rotate (Fig. 2d) and slide along the axial direction (Fig. 3), maximizing the formation of new H-bonds. Notably, the water cluster in the 1.0d-CNT model exhibits a clear uniaxial rotation shortly after 5 ps.

Notably, Fig. 2c shows the temporal evolution of the dipole moment for water molecules confined within different CNTs. A significant majority of water molecules in each CNT achieve complete dipole moment alignment within 0.7 ps. After 10 ps, the N_{HB} stabilizes at approximately 0.89 for 0.6d-CNT model, indicating that the water structure has reached stability. During this period, the water structure exerts no force on the capsule (Fig. 2b). As illustrated in Fig. 2b, the hydrodynamic force exerted by the water on the capsule becomes negligible after 10 ps, resulting in the maximum exit velocity (v_{out}) of the capsule, which is calculated

as the mean value of the axial centroid velocity (v_c) over the interval of [80, 100] ps. The figure inserted in Fig. 2b shows that the existence of a maximum electric field intensity (labeled as E_{CMax}) that can efficiently increase the v_{out} of the capsule within a given CNT. For example, the v_{out} rises rapidly when E is between 2.3 and 4.0 V/Å, as well as between 8.0 and 8.4 V/Å for the capsule in the 0.4d-CNT model. When E exceeds 8.4 V/Å, v_{out} changes minimally, indicating that E_{CMax} for the 0.4d-CNT model is 8.4 V/Å. For capsules in barrels with larger diameters, both v_{out} and the corresponding E_{CMax} decrease (see Table S3).

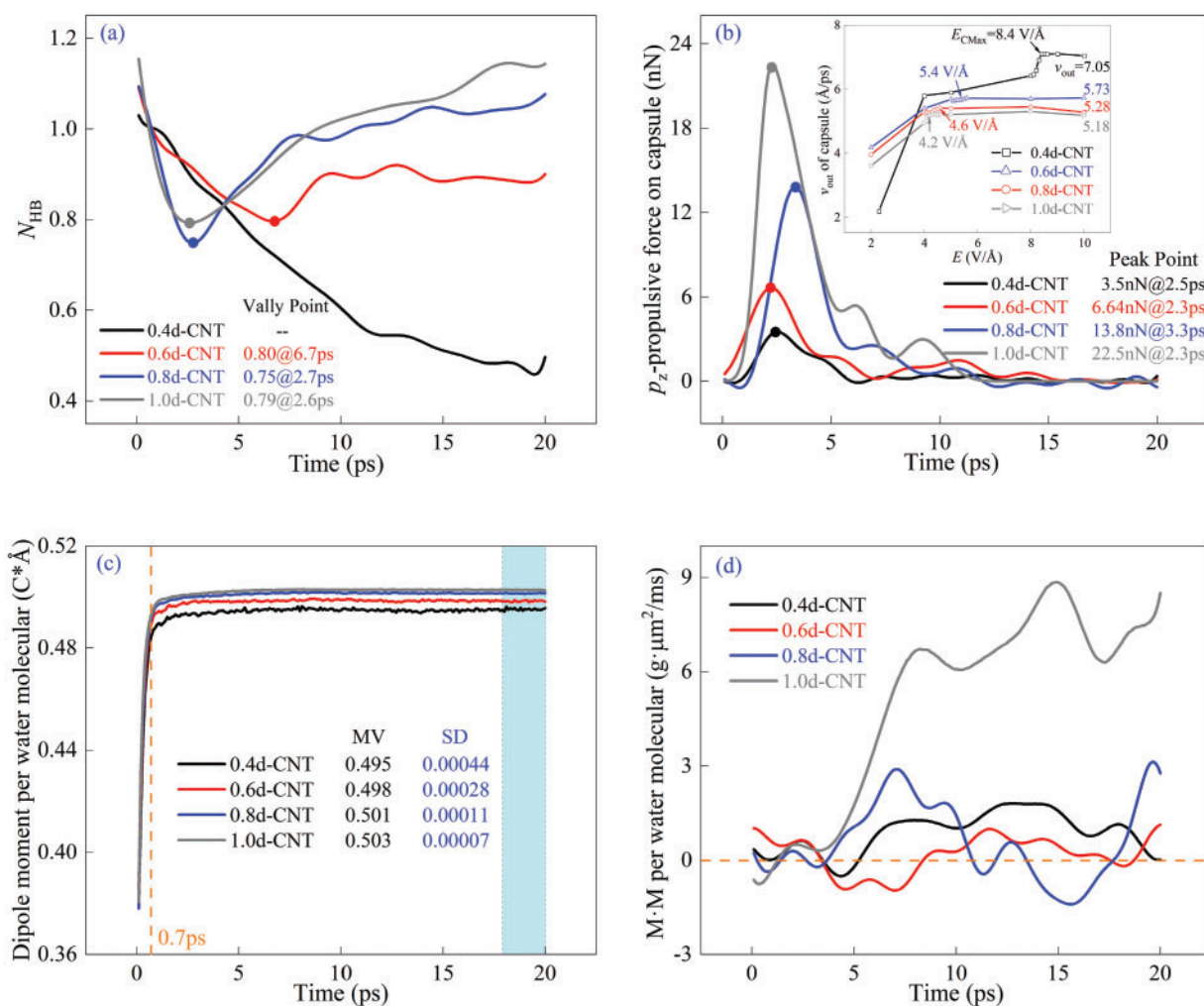


Figure 2: Responses of the four models at 300 K when turning on the electric field with $E = 5 \text{ V/\AA}$ and $s = 20 \text{ ps}$. (a) Evolution of the number of hydrogen bonds (H-bonds) per water molecular (N_{HB}); (b) The histories of the propulsive force on the capsule; The exit velocity (v_{out}) of the nanocapsule versus the EF intensity in different barrels at 300 K are inset; (c) Dipole moment per water molecular in the CNT, the mean value (MV) and standard deviation (SD) in each case is collected between 18 and 20 ps; (d) The moment of momentum ($M \cdot M$) per water molecular about the tube axis

To further elucidate the changes in the topological structure of H-bonds within water molecules and the reorientation of their dipole moments induced by the external EF, we analyzed the evolution of the water structure in both the side and top views of the 0.6d-CNT model at 300 K when the EF is activated at $E = 5 \text{ V/\AA}$ (see Fig. 3). Four local H-bond structures and dipole moments are illustrated in Fig. 3, with oxygen atoms shown in red, hydrogen atoms in blue, and blue arrows indicating the direction of the dipole

moments (p) of the water molecules. It can be observed that the external EF induces a transition in the dipole moments of water molecules from a disordered distribution to a uniform arrangement, accompanied by the reorganization of H-bonds. For instance, at 0 ps, when the external EF is off, the dipole moments are randomly distributed. Upon applying the EF at $E = 5 \text{ V/\AA}$, the dipole moments of the water molecules rapidly reorient, as depicted in Fig. 2c. After 2 ps, the dipole moments are completely aligned with the direction of the EF. During the reorganization of the H-bonds and the reorientation of dipole moments, water molecules progressively migrate toward the inner surface of the CNT, forming an internal pore within the water cluster. As the water layer becomes thinner, axial expansion occurs, which subsequently drives the capsule out of the CNT, resulting in a significantly larger v_{out} .

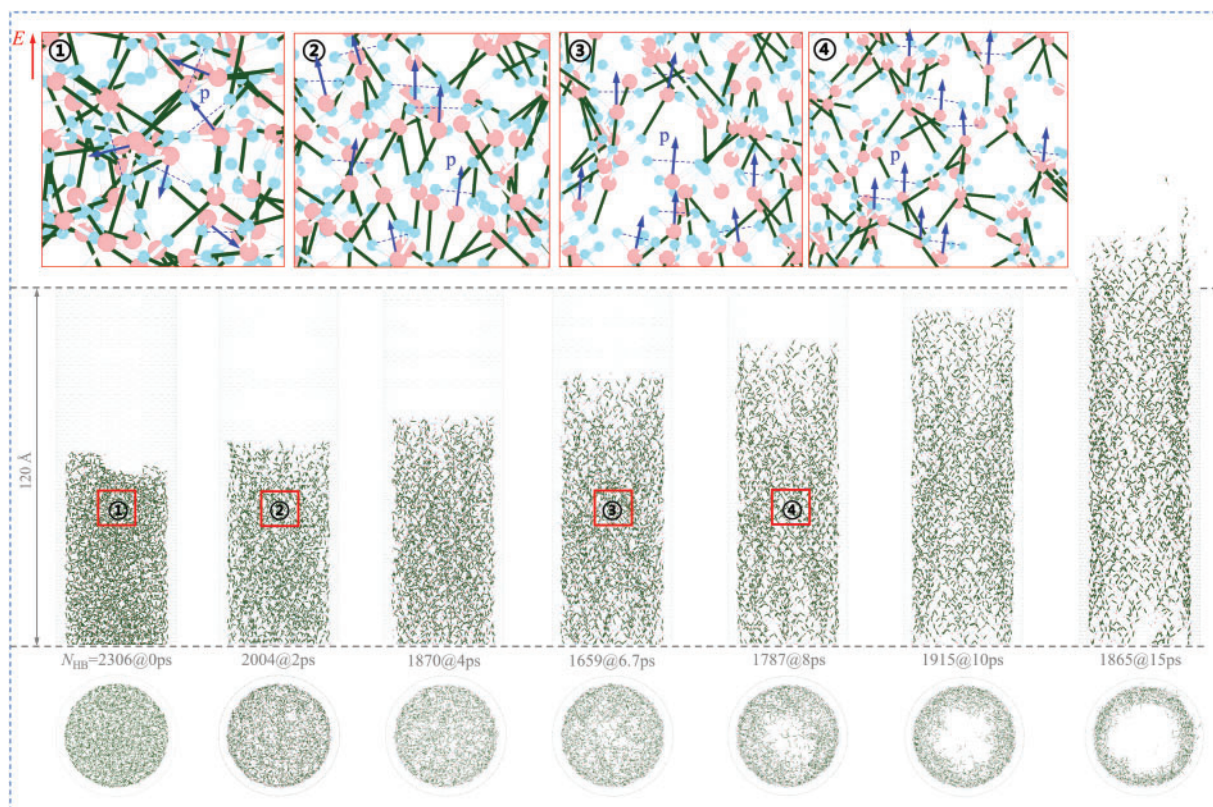


Figure 3: Evolution of the water structure in the 0.6d-CNT model at 300 K when turning on the EF with $E = 5 \text{ V/\AA}$ and $s = 20 \text{ ps}$. The number of H-bonds at each moment is listed between the side view and axial view of the system. Local layouts of the H-bonds and the dipole moments (p) are inserted

Each water molecule in a CNT exhibits four independent and distinct motions when subjected to a strong EF: self-rotation about its own dipole, rigid rotation about the tube axis, linear sliding along the tube axis, and radial motion toward the CNT surface. To illustrate these motions, Fig. 4 shows a selected molecule in the 0.6d-CNT model undergoing all four movements. Fig. 2d indicates that in a CNT with a larger diameter, the water cluster rotates more rapidly, increasing the number of water molecules that approach the inner wall of the CNT. This leads to the formation of a thinner water layer (see Fig. 3). Blue pentagons in Fig. 4 label the selected water molecule at different time points to demonstrate these motions. The rotation of the molecule is illustrated by the variation of the first two components of the unit vector d_p (Fig. 4), while the third component of d_p approaches 1.0, indicating the alignment of the dipole moment with

the direction of the EF. As water molecules undergo rotation, translation, and axial sliding, they engage in the formation of additional H-bonds with neighboring molecules, ultimately resulting in the establishment of a stable and organized H-bond network. During this process, the water clusters provide a stable driving force to the capsule effectively propelling it out of the CNT.

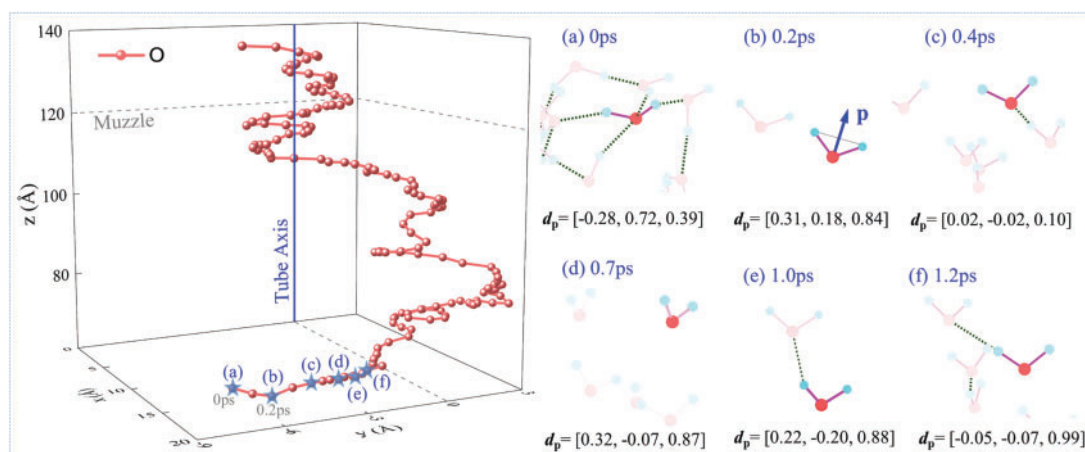


Figure 4: Snapshots and trajectory diagram of a selected water molecular in the 0.6d-CNT at 300 K in the EF with $E = 5 \text{ V}/\text{Å}$ and $s = 20 \text{ ps}$. Unit vector \mathbf{d}_p indicates the direction of the dipole moment (\mathbf{p}) of the selected molecular with local H-bond environments at different moments

To gain a deeper understanding of the deformation of water clusters in CNTs of different diameters and their impact on the value of v_{out} , we collected representative snapshots of the systems with 0.4d-CNT and 1.0d-CNT models while applying an EF of $E = 5 \text{ V}/\text{Å}$ for 20 ps. As illustrated in Fig. 5a, the tube diameter in the 0.4d-CNT model is 27.1 Å ($< 30 \text{ Å}$). Due to this size constraint, the water molecules in the narrower CNT are unable to effectively separate and form an internal pore, which leads to the axial expansion of more water molecules. This prevents the establishment of a continuous H-bond network, ultimately providing a high, sustained driving force for the capsule. Consequently, under the same EF conditions, the water clusters within

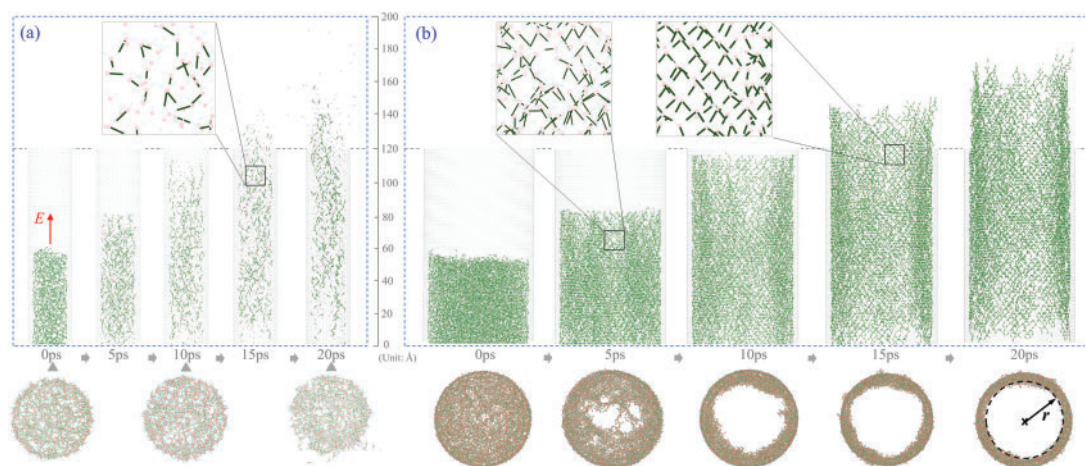


Figure 5: Top and side views of the H-bond structure in water clusters at different moments at 300 K in different CNTs in the EF with $E = 5 \text{ V}/\text{Å}$ and $s = 20 \text{ ps}$. (a) 0.4d-CNT and (b) 1.0d-CNT. Note that the diameters of the two tubes are 27.1 Å and 67.8 Å , respectively. Local layouts of the H-bonds are inserted

the 0.4d-CNT model achieve a maximum $v_{\text{out}} = 5.84 \text{ \AA/ps}$ for the capsule among the four cases examined (see Fig. S1).

For models with CNT diameters greater than 40 \AA , such as the 1.0d-CNT and 0.6d-CNT as shown in Fig. 3, the water clusters have the potential to form an internal pore. As the water cluster expands along the tube axis, the molecules simultaneously move toward the tube wall, and the rearrangement of H-bonds leads to a more organized H-bond network. In larger CNTs, the water cluster creates a larger internal pore, resulting in a thinner water shell that reduces the effective impact area of the water cluster on the capsule. Consequently, the water cluster within a 0.6d-CNT can provide a higher v_{out} to the capsule compared to those in the 0.8d-CNT and 1.0d-CNT models. For instance, v_{out} is 5.68 \AA/ps for the 0.6d-CNT model, 5.43 \AA/ps for the 0.8d-CNT model and 5.21 \AA/ps for the 1.0d-CNT model.

To quantitatively describe the deformation of the water cluster, we calculated the number density of water molecules along the radial direction in a CNT, as illustrated in Fig. 6. In the 0.4d-CNT model, the number density of water molecules across different cylindrical shells shows no significant variation, indicating a uniform distribution within the CNT. As a result, the formation of an internal pore within the water cluster does not occur. In contrast, the 0.6d-CNT model exhibits a relatively stable number density of water molecules during the initial 5 ps. After this period, the water molecules gradually move toward the tube wall to form a pore, reaching a radius of approximately 7 \AA at 10 ps (see Fig. S1b). For the 0.8d-CNT and 1.0d-CNT models, the radii of the pores at 10 ps are 9 and 16 \AA , respectively. Consequently, the ratio of the pore area to the cross-sectional area of the CNT is higher for larger diameters, with values of 0.33 for the 0.8d-CNT and 0.47 for the 1.0d-CNT models. Due to a smaller contact area and a slower rate of axial expansion, the water cluster can only provide a lower exit velocity for the capsule (see Fig. 2b). Additionally, the number density near the CNT wall drops steeply to zero because of a vacuum layer that forms between the inner surface of the CNT and the water cluster.

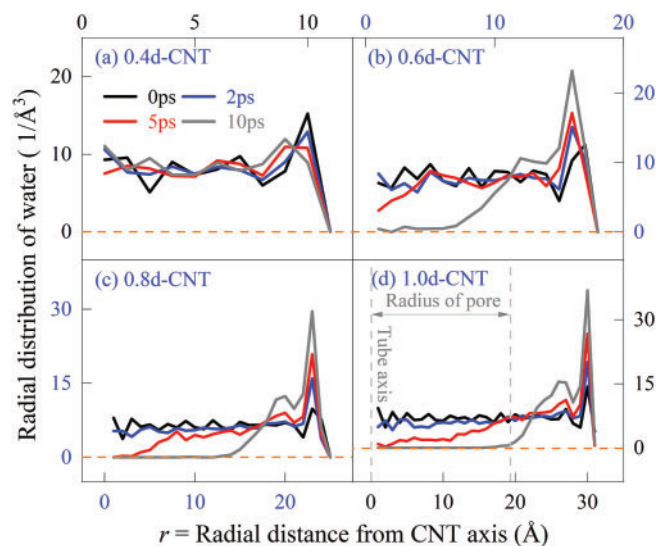


Figure 6: Radial distribution of water molecules ($N(r)/V(r)$) about the tube axis of a CNT, where $N(r)$ is the total number of water molecules in the cylinder shell with radius of r and thickness of $\Delta r = 1 \text{ \AA}$, and $V(r)$ is the volume of the concentric cylinder shell. The four models sink in the same EF with $E = 5 \text{ V/\AA}$ and $s = 20 \text{ ps}$: (a) 0.4d-CNT, (b) 0.6d-CNT, (c) 0.8d-CNT, and (d) 1.0d-CNT

3.2 Effect of the Water Depth in CNT

In the previous discussion, the water depth in the CNT was kept constant at $H = 70 \text{ \AA}$. Now, we consider how variations in water depth H varies within the same CNT, which correspond to different numbers of water molecules, affect the structural evolution of the water cluster. To investigate this effect, we varied the number of water molecules in the same CNT, specifically the 0.6d-CNT. For instance, the number of water molecules is 1536 when $H = 50 \text{ \AA}$, 1841 when $H = 60 \text{ \AA}$, 2131 when $H = 70 \text{ \AA}$, and 2423 when $H = 80 \text{ \AA}$.

Fig. 7 shows the value of N_{HB} within the water clusters and the driving force exerted on the capsule for various values of H when the EF is applied with $E = 5 \text{ V/\AA}$ for 20 ps. During the first 6.5 ps, the N_{HB} values in each water cluster decrease, disrupting the original H-bond network. During this period, the water cluster expands axially along the tube, generating the driving force for the capsule. After approximately 6.5 ps, while the water cluster continues expanding, it begins to move towards the barrel wall and the H-bond network starts to reform. Throughout this process, the axial force exerted by the water cluster on the bullet initially increases but then gradually decreases to zero. Slight differences in the descent paths before 5 ps can be observed. When $H = 50 \text{ \AA}$, the force exerted on the capsule reaches its peak, resulting in the maximum v_{out} . In contrast, when $H = 60 \text{ \AA}$, although the peak force is lower, the increased distance and duration of acceleration provide a higher v_{out} , compared to models with $H > 60 \text{ \AA}$. Notably, when $H \leq 60 \text{ \AA}$, the driving force on the capsule does not start from zero, as the water cluster is already in contact with the capsule after relaxation, generating force even before the EF is applied. Conversely, for $H > 60 \text{ \AA}$, a gap between the relaxed water cluster and the capsule exists (see the inset in Fig. 7b), resulting in a delayed application of the driving force.

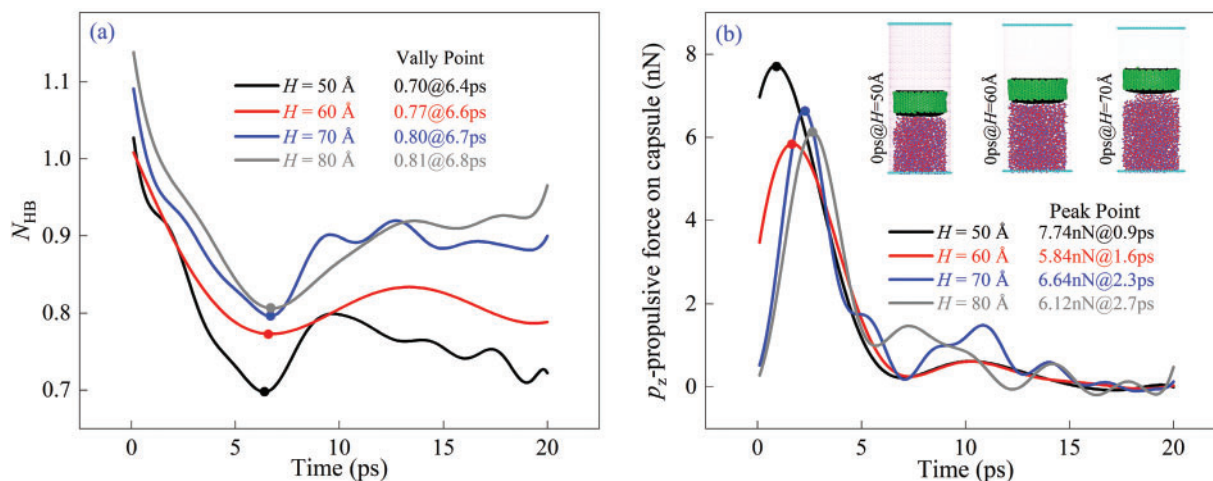


Figure 7: Responses of the 0.6d-CNT model with different depths of water at 300 K when turning on the EF with $E = 5 \text{ V/\AA}$ and $s = 20 \text{ ps}$. (a) The number of H-bonds per water molecular (N_{HB}); (b) The propulsive force on the capsule

The top views of the H-bond structures within the same CNT under the same EF are given in Fig. 8. By comparing the distribution of water molecules, one can see that an increased number of water molecules in the given CNT results in a smaller radius for the circular pore within the water cluster. For instance, when $H = 50 \text{ \AA}$, the water molecules show a low filling density within CNT and are distributed sparsely, forming a larger internal pore; however, when H increases to 80 \AA , the filling density of water molecules rises significantly, resulting in a notably reduced radius of the internal pore. As the water depth within the CNT rises, an excessive number of water molecules lead to spatial congestion, restricting radial migration and consequently influencing pore formation. Hence, a greater water depth can give rise to a smaller internal

pore. Consequently, the effective contact area between the water and the capsule increases, enabling the capsule to achieve a convergent v_{out} with a weaker EF (Fig. S3).

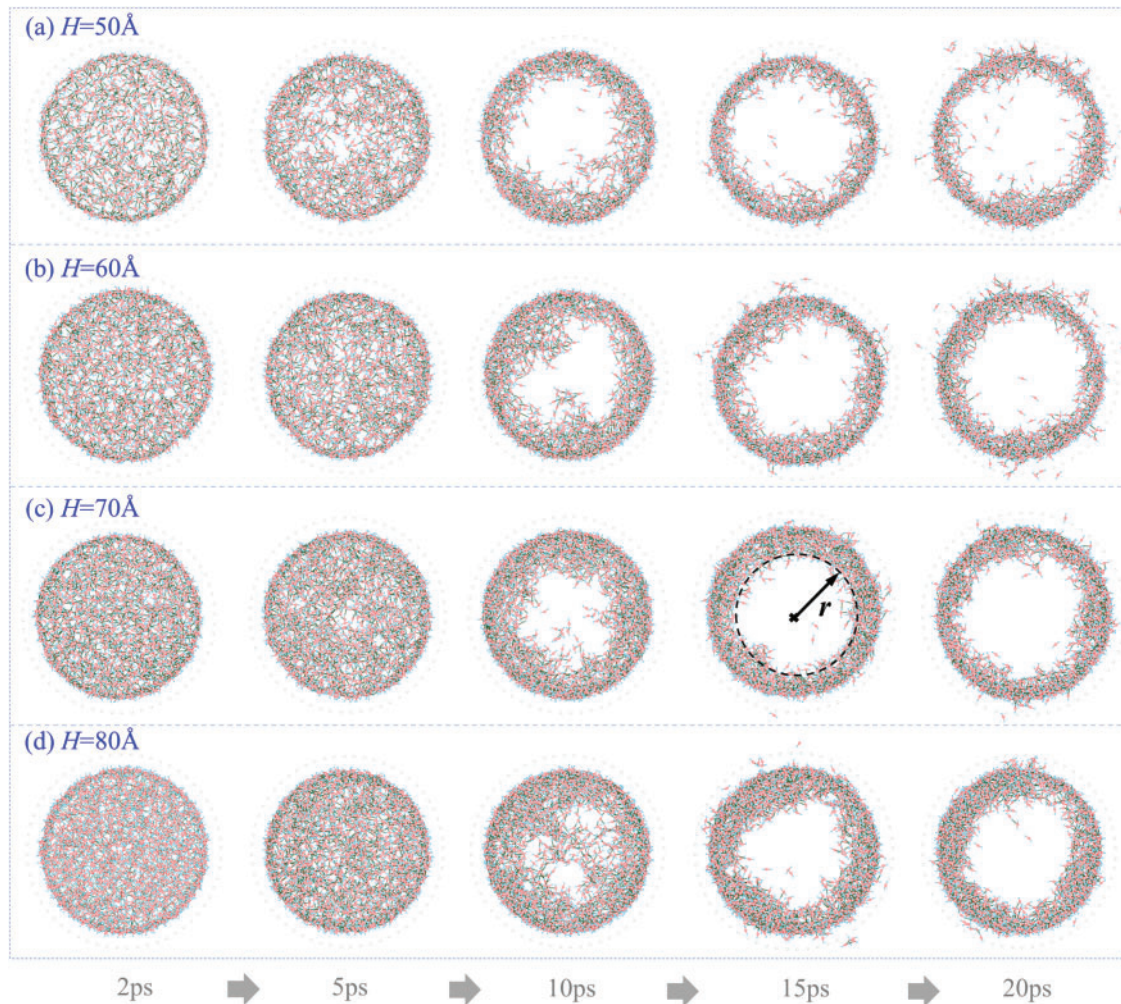


Figure 8: Representative top views of the H-bond structures in the water clusters in the 0.6d-CNT when turning on the EF with $E = 5 \text{ V}/\text{\AA}$ and $s = 20 \text{ ps}$ at 300 K. (a) $H = 50 \text{ \AA}$; (b) $H = 60 \text{ \AA}$; (c) $H = 70 \text{ \AA}$; and (d) $H = 80 \text{ \AA}$

4 Conclusions

On the nanoscale, a crucial step in mass transfer is achieving controlled motion for nanoparticles. We evaluated the unidirectional explosion of finite volume water confined within a single-end-opened CNT via MD simulation. The explosion is stimulated by an external pulsed EF. The effects of barrel diameter (αd) and water depth (H) on the structural evolution of the water cluster during the explosion were demonstrated through simulations, leading to the following conclusions:

Firstly, the explosion behavior of a given water cluster depends on the CNT diameter, e.g., when the diameter is less than 30 \AA , the water cluster containing fewer molecules expands primarily along the axial direction, otherwise, the water cluster forms an internal pore during axial expansion in a wider CNT.

Secondly, for the same water depth H , when the CNT is narrower and subjected to an EF with intensity $E > E_{CMin}$ (the value required for the capsule to escape from the CNT), the water cluster produces a higher exit velocity (v_{out}).

Finally, for a given model, v_{out} is higher when the water depth H is lower. This occurs because the axial expansion of the water cluster spends more time on accelerating the capsule, significantly increasing its v_{out} .

These findings offer theoretical insights for potential applications of directional explosion of nanofluids for nanoscale mass transfer, e.g., in nanofabrications and bioengineering. Specifically, within the domain of nanomanufacturing, it can be utilized in the nanoscale 3D printing procedure. The high pressure engendered by explosions can facilitate the directional deposition of nanoparticles, attaining precise structural construction. Concerning drug delivery, controllable drug release can be accomplished. Drugs can be encapsulated in nanocapsules and undergo directional explosion triggered by an external electric field, thereby allowing the targeted release of drugs in specific tissue or cellular environments.

Acknowledgement: Not applicable.

Funding Statement: The Start-up Research Fund from Shenzhen, the Natural Science Foundation of Guangdong (Grant Nos. 2024A1515010821, 2025A1515011727), and the Shenzhen Development and Reform Commission (Grant No. XMHT20220103004).

Author Contributions: Conceptualization, Kun Cai; methodology, Yuanyuan Kang, Jiahao Liu and Haiyan Duan; software, Jiahao Liu and Yuanyuan Kang; formal analysis, Jiahao Liu, Yuanyuan Kang, Kun Cai, Haiyan Duan and Jiao Shi; investigation, Yuanyuan Kang, Haiyan Duan and Jiao Shi; resources, Kun Cai; data curation, Yuanyuan Kang, Jiahao Liu and Haiyan Duan; writing—original draft preparation, Jiahao Liu, Yuanyuan Kang, Kun Cai, Haiyan Duan and Jiao Shi; writing—review and editing, Kun Cai and Jiao Shi; supervision, Kun Cai; project administration, Jiao Shi; funding acquisition, Kun Cai. All authors reviewed the results and approved the final version of the manuscript.

Availability of Data and Materials: Data available on request from the authors.

Ethics Approval: Not applicable.

Conflicts of Interest: The authors declare no conflicts of interest to report regarding the present study.

Supplementary Materials: The supplementary material is available online at <https://www.techscience.com/doi/10.32604/cmc.2025.066249/sl>.

References

1. Hao R, Yu ZT, Du J, Hu S, Yuan C, Guo H, et al. A high-throughput nanofluidic device for exosome nanoporation to develop cargo delivery vehicles. *Small*. 2021;17(35):e2102150. doi:10.1002/sml.202102150.
2. Wunsch BH, Smith JT, Gifford SM, Wang C, Brink M, Bruce RL, et al. Nanoscale lateral displacement arrays for the separation of exosomes and colloids down to 20 nm. *Nat Nanotechnol*. 2016;11(11):936–40. doi:10.1038/nnano.2016.134.
3. Franceschini L, Soskine M, Biesemans A, Maglia G. A nanopore machine promotes the vectorial transport of DNA across membranes. *Nat Commun*. 2013;4(1):2415. doi:10.1038/ncomms3415.
4. Wang J, Song ZY, He ML, Qian YC, Wang D, Cui Z, et al. Light-responsive and ultrapermeable two-dimensional metal-organic framework membrane for efficient ionic energy harvesting. *Nat Commun*. 2024;15(1):2125. doi:10.1038/s41467-024-46439-w.
5. Zhang Z, Wen LP, Jiang L. Nanofluidics for osmotic energy conversion. *Nat Rev Mater*. 2021;6(7):622–39. doi:10.1038/s41578-021-00300-4.

6. Guan KC, Guo YA, Li Z, Jia YD, Shen Q, Nakagawa K, et al. Deformation constraints of graphene oxide nanochannels under reverse osmosis. *Nat Commun.* 2023;14(1):1016. doi:10.1038/s41467-023-36716-5.
7. Nazari M, Davoodabadi A, Huang DZ, Luo TF, Ghasemi H. Transport phenomena in nano/molecular confinements. *ACS Nano.* 2020;14(12):16348–91. doi:10.1021/acsnano.0c07372.
8. Khatibi M, Mojavezi A, Pourjafarabadi E. Harvesting blue energy: pH-regulated nanochannels inspired by carbon nanostructures. *Phys Fluids.* 2023;35(10):102017. doi:10.1063/5.0170927.
9. Bran C, Berganza E, Fernandez-Roldan JA, Palmero EM, Meier J, Calle E, et al. Magnetization ratchet in cylindrical nanowires. *ACS Nano.* 2018;12(6):5932–9. doi:10.1021/acsnano.8b02153.
10. Hui Y, Yi X, Hou F, Wibowo D, Zhang F, Zhao DY, et al. Role of nanoparticle mechanical properties in cancer drug delivery. *ACS Nano.* 2019;13(7):7410–24. doi:10.1021/acsnano.9b03924.
11. Zhuang J, Kuo CH, Chou LY, Liu DY, Weerapana E, Tsung CK. Optimized metal-organic-framework nanospheres for drug delivery: evaluation of small-molecule encapsulation. *ACS Nano.* 2014;8(3):2812–9. doi:10.1021/nn406590q.
12. Esfandiar A, Radha B, Wang FC, Yang Q, Hu S, Garaj S, et al. Size effect in ion transport through angstrom-scale slits. *Science.* 2017;358(6362):511–3. doi:10.1126/science.aan5275.
13. Shen J, Liu GP, Han Y, Jin WQ. Artificial channels for confined mass transport at the sub-nanometre scale. *Nat Rev Mater.* 2021;6(4):294–312. doi:10.1038/s41578-020-00268-7.
14. Heydari A, Khatibi M, Ashrafizadeh SN. Smart nanochannels: tailoring ion transport properties through variation in nanochannel geometry. *Phys Chem Chem Phys.* 2023;25(39):26716–36. doi:10.1039/D3CP03768A.
15. Takakura A, Beppu K, Nishihara T, Fukui A, Kozeki T, Namazu T, et al. Strength of carbon nanotubes depends on their chemical structures. *Nat Commun.* 2019;10(1):3040. doi:10.1038/s41467-019-10959-7.
16. Mukunda SG, Boppana SB, Palani IA, Dayanand S, Aravinda T. Characterisation of AZ31 metal matrix composites reinforced with carbon nanotubes. *Sci Rep.* 2023;13(1):17786. doi:10.1038/s41598-023-44719-x.
17. Raju M, van Duijn A, Ihme M. Phase transitions of ordered ice in graphene nanocapillaries and carbon nanotubes. *Sci Rep.* 2018;8(1):3851. doi:10.1038/s41598-018-22201-3.
18. Secchi E, Marbach S, Niguès A, Stein D, Siria A, Bocquet L. Massive radius-dependent flow slippage in carbon nanotubes. *Nature.* 2016;537(7619):210–3. doi:10.1038/nature19315.
19. Tunuguntla RH, Henley RY, Yao Y, Pham TA, Wanunu M, Noy A. Enhanced water permeability and tunable ion selectivity in subnanometer carbon nanotube porins. *Science.* 2017;357(6353):792–6. doi:10.1126/science.aan2438.
20. Hummer G, Rasaiah JC, Noworyta JP. Water conduction through the hydrophobic channel of a carbon nanotube. *Nature.* 2001;414(6860):188–90. doi:10.1038/35102535.
21. Majumder M, Chopra N, Andrews R, Hinds BJ. Nanoscale hydrodynamics-Enhanced flow in carbon nanotubes. *Nature.* 2005;438(7064):44. doi:10.1038/438044a.
22. Rinne KF, Gekle S, Bonthuis DJ, Netz RR. Nanoscale pumping of water by AC electric fields. *Nano Lett.* 2012;12(4):1780–3. doi:10.1021/nl203614t.
23. Lv F, Fang C, Su J. Enhanced water transport through a carbon nanotube controlled by the lateral pressure. *Nanotechnol.* 2019;30(24):245707. doi:10.1088/1361-6528/ab0cd7.
24. Thomas JA, McGaughey AJH. Water flow in carbon nanotubes: transition to subcontinuum transport. *Phys Rev Lett.* 2009;102(18):184502. doi:10.1103/PhysRevLett.102.184502.
25. Holt JK, Park HG, Wang YM, Stadermann M, Artyukhin AB, Grigoropoulos CP, et al. Fast mass transport through sub-2-nanometer carbon nanotubes. *Science.* 2006;312(5776):1034–7. doi:10.1126/science.1126298.
26. Kalra A, Garde S, Hummer G. Osmotic water transport through carbon nanotube membranes. *Proc Natl Acad Sci U S A.* 2003;100(18):10175–80. doi:10.1073/pnas.1633354100.
27. Thomas JA, McGaughey AJH. Reassessing fast water transport through carbon nanotubes. *Nano Lett.* 2008;8(9):2788–93. doi:10.1021/nl8013617.
28. Wan ZY, Gao YR, Chen XY, Zeng XC, Francisco JS, Zhu CQ. Anomalous water transport in narrow-diameter carbon nanotubes. *Proc Natl Acad Sci U S A.* 2022;119(39):e2211348119. doi:10.1073/pnas.2211348119.
29. Srivastava A, Hassan J, Homouz D. Effect of size and temperature on water dynamics inside carbon nano-tubes studied by molecular dynamics simulation. *Molecules.* 2021;26(20):6175. doi:10.3390/molecules26206175.

30. Arrhenius S. Über die reaktionsgeschwindigkeit bei der inversion von rohrzucker durch säuren. *Z Für Phys Chem*. 1889;4(1):226–48. doi:10.1515/zpch-1889-0416.
31. Song JS, Liu L, Li QB, Liu C, Song FH. Entrance resistance of water transport into carbon nanotubes: insights from molecular dynamics simulations. *J Mol Liq*. 2021;331:115739. doi:10.1016/j.molliq.2021.115739.
32. Zimmerli U, Gonnet PG, Walther JH, Koumoutsakos P. Curvature induced-defects in water conduction in carbon nanotubes. *Nano Lett*. 2005;5(6):1017–22. doi:10.1021/nl0503126.
33. Su JY, Guo HX. Control of unidirectional transport of single-file water molecules through carbon nanotubes in an electric field. *ACS Nano*. 2011;5(1):351–9. doi:10.1021/nn1014616.
34. Zhu JZ, Lan YQ, Du HJ, Zhang YH, Su JG. Tuning water transport through nanochannels by changing the direction of an external electric field. *Phys Chem Chem Phys*. 2016;18(27):17991–6. doi:10.1039/C6CP00610H.
35. Hadidi H, Kamali R. Non-equilibrium molecular dynamics simulations of water transport through plate- and hourglass-shaped CNTs in the presence of pressure difference and electric field. *Comput Mater Sci*. 2020;185(6):109978. doi:10.1016/j.commatsci.2020.109978.
36. Ge ZP, Shi YC, Li XY. Effects of orthogonal electric field on water flux through a carbon nanotube. *Acta Phys-Chim Sin*. 2013;29(8):1655–60. doi:10.3866/PKU.WHXB201305222.
37. Ostler D, Kannam SK, Frascoli F, Daivis PJ, Todd BD. Inducing a net positive flow of water in functionalized concentric carbon nanotubes using rotating electric fields. *Langmuir*. 2019;35(45):14742–9. doi:10.1021/acs.langmuir.9b02594.
38. Cai K, Wu P, Shi J, Zhong Z, Zhang Y. CNT-motor driven by competition between thermal fluctuation and REF. *Int J Mech Sci*. 2022;225:107372. doi:10.1016/j.ijmecsci.2022.107372.
39. Kang Y, Duan H, Liu J, Shi J, Qin QH. The viscosity-propelled rotary nanomotor through the solid-liquid interface. *J Nano Res*. 2024;84:41–5. doi:10.4028/p-W7hOUi.
40. Salman S, Zhao YZ, Zhang XK, Su JY. Effect of temperature on the coupling transport of water and ions through a carbon nanotube in an electric field. *J Chem Phys*. 2020;153(18):184503. doi:10.1063/5.0028077.
41. Kang Y, Cai K, Shi J, Luo Y, Zhang Y. CNT-based nanogun triggered by an EF. *Comput Mater Sci*. 2023;228(6):112305. doi:10.1016/j.commatsci.2023.112305.
42. Duan H, Liu J, Kang Y, Cai K, Shi J, Qin QH. Effects of a pulsed electric field on the ejection of an electric-neutral nanocapsule out of a water-filled CNT barrel. *J Mol Liq*. 2024;407(9):125280. doi:10.1016/j.molliq.2024.125280.
43. Plimpton S. Fast parallel algorithms for short-range molecular-dynamics. *J Comput Phys*. 1995;117(1):1–19. doi:10.1006/jcph.1995.1039.
44. Berendsen HJC, Grigera JR, Straatsma TP. The missing term in effective pair potentials. *J Phys Chem*. 1987;91(24):6269–71. doi:10.1021/j100308a038.
45. Gonnet P. P-SHAKE: a quadratically convergent SHAKE in $O(n^2)$. *J Comput Phys*. 2007;220(2):740–50. doi:10.1016/j.jcp.2006.05.032.
46. Stuart SJ, Tutein AB, Harrison JA. A reactive potential for hydrocarbons with intermolecular interactions. *J Chem Phys*. 2000;112(14):6472–86. doi:10.1063/1.481208.
47. Moucka F, Nezbeda I. Water-methanol mixtures with non-Lorentz-Berthelot combining rules: a feasibility study. *J Mol Liq*. 2011;159(1):47–51. doi:10.1016/j.molliq.2010.05.005.
48. Werder T, Walther JH, Jaffe RL. On the water-carbon interaction for use in molecular dynamics simulations of graphite and carbon nanotubes. *J Phys Chem B*. 2003;107(6):1345–52. doi:10.1021/jp0268112.
49. Nosé S. A unified formulation of the constant temperature molecular dynamics methods. *J Chem Phys*. 1984;81(1):511–9. doi:10.1063/1.447334.
50. Kumar R, Schmidt JR, Skinner JL. Hydrogen bonding definitions and dynamics in liquid water. *J Chem Phys*. 2007;126(20):204107. doi:10.1063/1.2742385.